Magnetic proximity coupling to defects in a two-dimensional semiconductor

Muhammad Hassan Shaikh,[†] Matthew P. Whalen,[‡] Dai Q. Ho,[¶,§] Aqiq Ishraq,[¶] Collin Maurtua,[¶] Kenji Watanabe,[‖] Takashi Taniguchi,[‖] Yafei Ren,[†] Anderson Janotti,[¶] John Q. Xiao,[†,‡] and Chitraleema Chakraborty[*,†,‡,¶]

†*Department of Physics, University of Delaware, Newark, Delaware, 19716, USA*

‡*Quantum Science and Engineering Program, University of Delaware, Newark, Delaware, 19716, USA*

¶*Department of Material Science and Engineering, University of Delaware, Newark, Delaware, 19716, USA*

§*Faculty of Natural Sciences, Quy Nhon University, Quy Nhon 55113, Vietnam*

‖*National Institute for Materials Science (NIMS) in Tsukuba, 305-0047, Japan*

E-mail: cchakrab@udel.edu

Phone: +1(302) 831-3251

Abstract

The ultrathin structure and efficient spin dynamics of two-dimensional (2D) antiferromagnetic (AFM) materials hold promising opportunities for ultrafast memory devices, artificial intelligence circuits, and advanced computing technology. For example, chromium thiophosphate ($CrPS_4$) is one of the most promising 2D A-type AFM materials due to its robust stability in diverse environmental conditions and net out-of-plane magnetic moment in each layer, attributed to anisotropy in crystal axes (a and b). However, their net-zero magnetic moment poses a challenge for detecting the Néel

state that is used to encode information. In this study, we demonstrate the detection of the Néel vector by detecting the magnetic order of the surface layer by employing localized defects in tungsten diselenide (WSe_2). These defects are ideal candidates for optically active transducers to probe the magnetic order due to their narrow linewidth and high susceptibility to magnetic field (B-fields). We observed spin-polarized charge transfer in the heterostructure of bulk $CrPS_4$ and single-layer WSe_2, indicating type-II band alignment as supported by density functional theory (DFT) calculations. In the A-type AFM regime, the intensity of both right-handed and left-handed circularly polarized light emanating from the sample remains constant as a function of the applied B-field, indicating a constant polarized transition behavior. Our results demonstrate an approach to optically characterizing the magnetic states of 2D bulk AFM material by using both localized and delocalized defect excitons as a probe, highlighting avenues for future research and technological applications.

Keywords: Two-dimensional magnet, Magnetic proximity effect, $CrPS_4$, WSe_2, defects in semiconductors, Spin-polarized charge transfer, Type-II band alignment.

Replacing ferromagnetic (FM) materials in commercial magnetic random-access memories (MRAMs)[1,2] and other applications such as artificial intelligence, neuromorphic computing, and in-memory computing[2,3] with AFM material holds the potential to improve the operation speed (from GHz to THz), the immunity to electromagnetic interference, and the memory density.[4–7] 2D AFM materials further push the limit to atomic layer thickness. The challenges are also daunting to implement AFM material-based devices since AFM materials nearly lack physical observables (resistance, voltage, etc.) that are related to their magnetic order parameter, known as the Néel vector.[2] Bringing the evident advantages of AFM materials into play by being able to detect the Néel vector would allow using their unique functionalities in future generations of advanced technologies.

Recently, binary transition metal chalcogenides (TMCs) have garnered significant attention due to their layer-dependent magnetic properties. Due to the van der Waals forces

between each layer, the material can be exfoliated down to a single layer that possesses a magnetic ground state, which enables the switching between FM and AFM material behavior, contingent upon the number of layers.[8,9] Chromium triiodide (CrI_3) is one of the binary TMCs that possess A-type AFM, with FM ordering within the same layer and AFM between adjacent layers. Consequently, thin flakes of a few layers can display a net or zero magnetic moment depending on whether there is an odd or even number of layers. The surface layer magnetic moment was successfully detected in the A-type AFM phase by utilizing another 2D optically active material, WSe_2, atop CrI_3.[10,11] WSe_2 possesses a valley-selective transition, and in the presence of a net out-of-plane B-field, the valley degeneracy can be lifted. Due to the high susceptibility of WSe_2 to the B-field, the surface layer magnetic moment of a magnetic material can be detected by measuring the energy splitting and observing differences in the intensity of valley transitions in WSe_2. However, CrI_3 is not stable in an open environment, which creates a problem in using this material in practical applications.[11]

Recently studied ternary TMCs $CrPS_4$ emerge as particularly noteworthy due to their stability in bulk form and high resonance capability, making them a viable candidate for advanced spintronic and memory device applications.[12–14] Notably, $CrPS_4$ exhibits an anisotropic crystal structure endowing each layer with net magnetic moments that are antiferromagnetically coupled, resulting in the same A-type AFM behavior as CrI_3.[12,13,15] This anisotropy extends to light absorption, rendering $CrPS_4$ suitable for polarization-based sensing and memory devices.[16,17]

However, its A-type AFM state in a bulk form with many layers that are antiferromagnetically coupled makes it difficult to sense the small change in the surface layer magnetization. To overcome this limitation, we propose integrating $CrPS_4$ with localized excitons in transition metal dichalcogenides (TMDCs) as a means to rectify surface layer magnetization, owing to their narrow linewidth relative to excitonic peaks, high excitonic g factor, and efficient electrical tunability.[18–28] Additionally, we present a method for detecting A-type AFM and canted antiferromagnetic (C-AFM) states using photoluminescence (PL) light po-

larization of bulk $CrPS_4$, providing insights into its magnetic behavior. We also observed constant polarized transition behavior from $CrPS_4$ in the A-type AFM regime. This constant polarized transition holds promise for potential applications in spintronics and ultrafast AFM-based memory devices. Our method not only enables the detection of surface layer magnetic moments but also provides valuable information about the various phases of antiferromagnetism present within bulk $CrPS_4$. While previous studies have focused on bulk excitons[10,11] and localized excitons,[29] our work extends this framework by also incorporating delocalized intrinsic defects as optical probes to study magnetic behavior via the magnetic proximity effect. This approach offers a comprehensive understanding of how free exciton and defect states (both localized and delocalized) can be harnessed to probe the magnetic properties of antiferromagnetic materials.

This work holds immense promise for advancing a wide range of technological applications, from data storage to tunable optical devices, and beyond.[11]

Results and discussion

In this study, we investigated the magnetic proximity interaction (MPI) between bulk $CrPS_4$ and single-layer WSe_2. Figure (Fig.) 1(a) shows a schematic of the magnetic heterostructure utilized for studying this interaction, where the magnetic material is closely interfaced with the optically active 2D semiconductor. The property of light emitted by the 2D semiconductor depends on the orientation of the surface layer magnetic moments within the magnetic material. This magnetic heterostructure could be utilized for potential ultrafast optical transduction. We have fabricated individual magnetic heterostructures with two kinds of defects (delocalized (intrinsic)[30] and localized[31]) in WSe_2 via annealing; the optical image of both heterostructures is shown in Fig. 1(b). The top image in Fig. 1(b) shows the magnetic heterostructure consisting of intrinsic defects, and the bottom image in Fig. 1(b) shows the magnetic heterostructure consisting of localized defects, which we referred

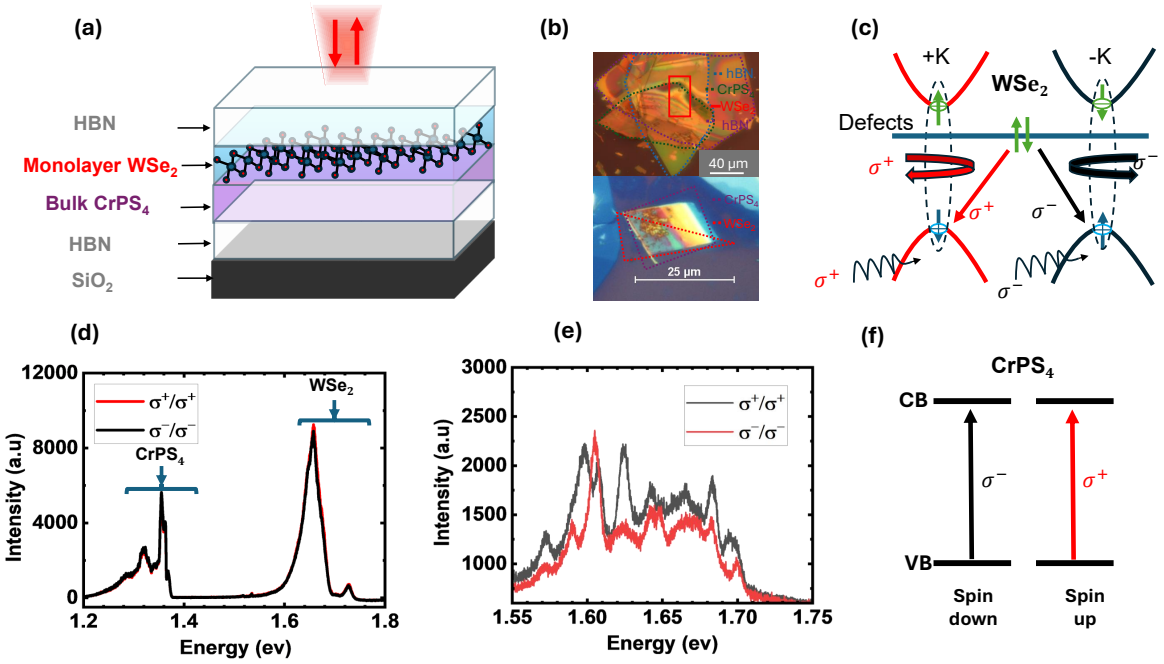


Figure 1: Low-temperature polarization-resolved PL of the $CrPS_4$ and WSe_2 heterostructure: (a) Schematic illustration of magnetic proximity interaction in the 2D system. (b) Optical image of $CrPS_4$ and WSe_2 heterostructure with hBN encapsulation (top) and without hBN encapsulation (bottom). (c), (f) Optical selection rules for WSe_2 and $CrPS_4$, respectively. (d) Co-polarization resolved PL of hBN encapsulated heterostructure revealing multiple peaks between 1.2-1.4 eV attributed to $CrPS_4$ due to vibrational progression. The peak centered around 1.65 eV corresponds to intrinsic defect states PL in WSe_2, and the 1.726 eV peak indicates the excitonic transition in WSe_2 at 1.8 K. (e) Co-polarization resolved PL of a sample without hBN encapsulation presenting multiple DBE in WSe_2 at 1.8 K.

to as defect-based bound excitons (DBE) in this work. Both bulk $CrPS_4$ (the magnetic material) and single-layer WSe_2 (optically active semiconductor) were mechanically exfoliated using the scotch tape method, and the heterostructure was assembled by stacking both flakes together employing a poly-carbonate (PC) assisted transfer technique,[32] with detailed procedures outlined in the methods section.

To study the valley-specific transitions,[33] we conducted co-polarization resolved PL measurements on the magnetic heterostructure, where the sample was excited with circularly polarized light (σ^+ or σ^-) and the emitted circularly polarized light (σ^+ or σ^-) was detected from the heterostructure. The selection rules for the optical transition in WSe_2 and $CrPS_4$ are illustrated in Fig. 1(c) and Fig. 1(f), respectively. We performed room tem-

perature polarization resolved PL spectroscopy (Supplementary Figure (S) 1) to understand the effects on excitonic transition in the paramagnetic phase of the heterostructure. In S1, the peak centered around 1.35 eV corresponds to the optical transition in $CrPS_4$, and the peak centered around 1.65 eV corresponds to optical transitions in WSe_2. We observed no evidence of MPI at room temperature, as the valley-specific transitions in WSe_2 remain energy-degenerate due to time-reversal symmetry. This is consistent with $CrPS_4$ being in a paramagnetic phase at this temperature. The valley degeneracy is only lifted in the presence of a B-field.

Next, we cooled the sample in a cryostat to 1.8 K, below the Néel temperature of $CrPS_4$ (37 K),[13] and measured the co-polarization-resolved PL of the heterostructure with intrinsic defects (Fig. 1(d)) and with DBE (Fig. 1(e)). Fig. 1(d) presents the PL spectrum of the heterostructure, where the PL contributions from $CrPS_4$ and WSe_2 are indicated. As previously observed, the multiple peaks in the $CrPS_4$ energy range can be attributed to a vibrational progression.[34] We extracted the peak energies of the intrinsic defect transition and the excitonic transition using Lorentzian fitting in S5. The peak centered around 1.65 eV corresponds to intrinsic defect states in WSe_2, representing an inhomogeneously broadened defect exciton originating from a high defect density.[30,35,36] The peak at 1.726 eV corresponds to A-excitonic transitions in WSe_2. The MPI can be characterized by measuring the degree of circular polarization/polarization contrast (ρ), which is given by:

$$\rho = \frac{I(\sigma^+/\sigma^+) - I(\sigma^-/\sigma^-)}{I(\sigma^+/\sigma^+) + I(\sigma^-/\sigma^-)} \tag{1}$$

The observed polarization contrast for intrinsic defects is $\sim$6%. We observe negligible polarization contrast from A-excitons. This effect can originate due to enhanced defect-mediated scattering of A-excitons in WSe_2 caused by high defect density, which suppresses polarization contrast.[36,37]

Next, we conducted the same experiment on a heterostructure consisting of $CrPS_4$ with

DBE in WSe_2. One of the photophysical signatures observed in spectroscopy in similar samples[22–26,28,31] is multiple optically active localized excitonic states with significantly narrower linewidths compared to the intrinsic defect states. Fig. 1(e) shows the polarization-resolved spectroscopy of such localized excitons in the magnetic heterostructure. Here, we observe finite circular polarization contrast and energy splitting between the σ^+/σ^+ and σ^-/σ^- PL spectra of DBE in WSe_2, even without an external B-field. The DBE are expected to exhibit purely linearly polarized emission at zero B-field due to anisotropic electron-hole exchange interactions in the presence of in-plane anisotropy.[38–41] To further verify that the DBE emits circularly polarized light, we excite the sample with linearly polarized (L) light and analyze the circularly polarized emission; if the defects lack magnetic interaction, no circular polarization contrast will appear under L-excitation. As seen in Fig. S9, the emission was indeed circularly polarized, and this polarization contrast gradually vanishes above the Néel temperature of $CrPS_4$ ($\sim$37 K) (See S8), though the polarization contrast was smaller than under co-polarized excitation, consistent with valley superposition formation during linearly polarized excitation.

The presence of finite polarization contrast in the PL spectrum of Fig. 1(e) is a signature of MPI between the surface layer of bulk $CrPS_4$ and single-layer WSe_2, even though the net magnetic moment is zero in bulk $CrPS_4$. MPI, being a short-range interaction, causes WSe_2 to experience a net out-of-plane magnetic moment from the surface layer of $CrPS_4$, leading to a finite polarization contrast at low temperatures without an external B-field. Such polarization contrast was previously observed in localized excitons of WSe_2 monolayers only when applying a Zeeman energy through an external B-field that overcomes the anisotropic Coulomb exchange interaction in localized excitons[22–25,38–41] or by coupling these emitters with chiral nanocavities.[42] We observe a similar polarization contrast that points to the restoration of valley polarization inherited from the 2D excitons in optically active defects in 2D semiconductors.[22–25,38–41]

In addition, we calculated the energy splitting magnitude for individual emitters from

Fig. 1(e) using Lorentzian fitting (see S6). The splitting magnitude varies between emitters (see S6(c)), and our position-dependent PL measurements reveal spatial variations across the heterostructure (see S10). This variability is expected, as these non-deterministically created DBE exhibit a distribution of g-factor values due to their differing microscopic origins.[22–25,38–41,43] This variation in g-factor across sample hinders the accurate extraction of the effective B-field from the Zeeman effect. However, despite the g-factor variation, the observed energy splitting values (see S6(c)) from most emitters are larger than the energy splitting usually observed in this type of emitters due to anisotropic Coulomb exchange interaction.[22–25,38–41,43] Such enhanced splitting was previously observed only under an external B-field, where Zeeman energy is used to overcome the anisotropic Coulomb exchange interaction in localized excitons. In our case (B-field=0), the Zeeman energy is instead provided by the $CrPS_4$ surface layer. Nevertheless, to isolate MPI effects in these DBE, we have focused on polarization contrast analysis. Zeeman splitting can be negligible for emitters with very low g-factors. However, polarization contrast always responds to B-fields.[43]

In order to isolate the magnetic interactions from temperature-dependent thermal effects, we next studied the influence of B-field on polarization contrast at a constant temperature of 1.8 K, which is below the phase transition temperature of the $CrPS_4$ bulk. Fig. 2(a) and 2(b) present the polarization resolved PL emission from $CrPS_4$ at $\pm$8.5 T (Faraday configuration). When the applied field aligns with the crystal -c-axis (-8.5 T), σ^- polarized emission dominated the PL from $CrPS_4$ (Fig. 2(a)) as most of the magnetic moment of $CrPS_4$ aligns with the direction of the B-field. Conversely, when we switched the B-field direction (8.5 T) and aligned it with the crystal +c-axis, σ^+ polarized emission dominated the PL from $CrPS_4$ (Fig. 2(b)), as most of the magnetic moment of $CrPS_4$ realigns with the +c-axis direction of the crystal.

However, both the intrinsic defect states in Fig. 2(d) and 2(e), and the DBE in Fig. 2(c) and 2(f), exhibit opposite polarization behavior compared to $CrPS_4$. When the B-field aligns along the +c-axis (-c-axis), the PL contribution is dominated by σ^- (σ^+) from both intrinsic

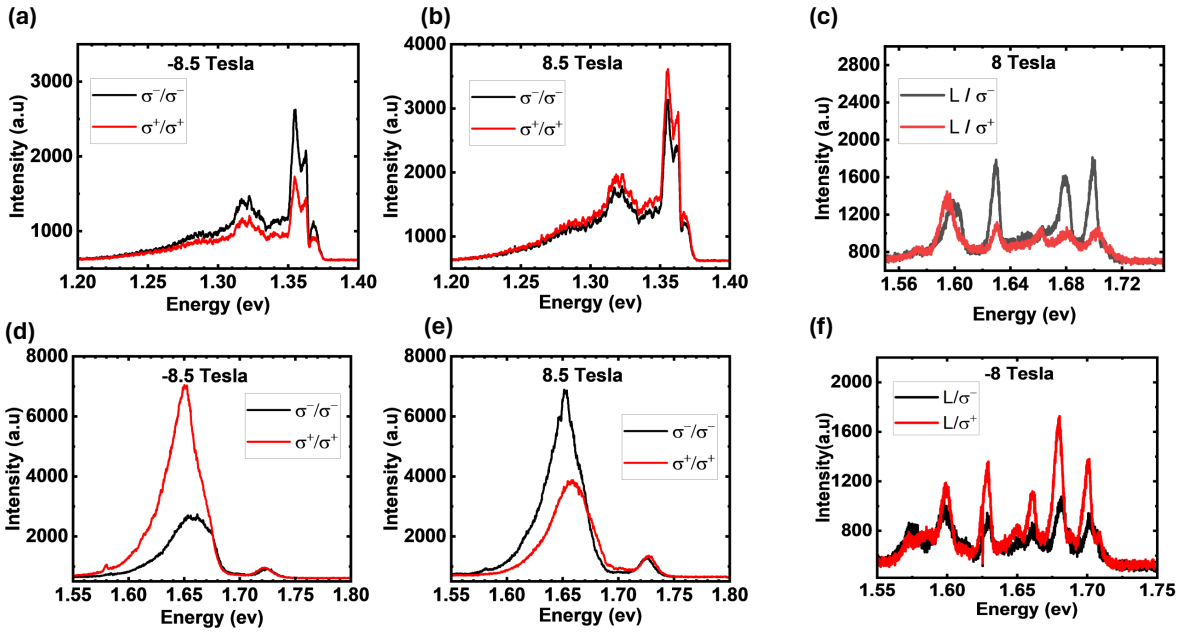


Figure 2: B-field-dependent PL of the heterostructure in Faraday's geometry: (a),(b) The PL contribution from $CrPS_4$ at high B-fields of ±8.5 Tesla. (d),(e) The PL contribution of intrinsic defects and A-excitons from WSe_2 under similar magnetic conditions as (a),(b). (c),(f) The PL contribution of DBE from WSe_2 excited by L-polarized light at B-fields of ± 8 Tesla.

defects and DBE.

We have calculated the ρ as a function of B-field for the $CrPS_4$ emission line at 1.355 eV (Fig. 3(a)). When $CrPS_4$ is in the A-type AFM state within the B-field range of ±0.8 T,[13] ρ remains non-zero but nearly constant (inset of Fig. 3(a)). For $|B| > 0.8$ T, $CrPS_4$ transitions into a spin-flop/C-AFM state,[13] resulting in increased ρ. In the C-AFM state, we observe unidirectional anisotropy in $\rho(B)$. Importantly, ρ does not show saturation behavior within our applied B-field range, suggesting the absence of a spin-flip transition. This lack of saturation also accounts for the absence of hysteresis in both ρ and energy splitting (ΔE) associated with the intrinsic defect peak in the magnetic heterostructure (Fig. 3(b),(c)).

Next, we have calculated ρ as a function of B-field for the intrinsic defect peak of WSe_2 centered at 1.65 eV (Fig. 3(b)). Notably, the behavior of ρ for $CrPS_4$ and WSe_2 exhibits an opposite trend with applied B-field. We also observed that when $CrPS_4$ is in the A-

type AFM state within the B-field range of ± 0.8 Tesla,[13] the ρ from $CrPS_4$ is non-zero but remains almost constant (inset of Fig. 3(a)), whereas the ρ from defect peak of WSe_2 increases linearly (inset of Fig. 3(b)).

This behavior can be understood through the Type-II band alignment and subsequent spin-selective charge transfer between $CrPS_4$ and WSe_2, as shown in Fig. 3(d). For B>0, electrons are only transferred from the +K valley of WSe_2 to $CrPS_4$, resulting in a decrease in the σ^+ transition compared to σ^- in the WSe_2 defect. Hence, a negative ρ is obtained at B>0 for the WSe_2 defect. Conversely, when we switch the B-field direction, the behavior also switches accordingly. We also observe a similar effect on ρ of DBE excitons in WSe_2 as shown in the color plot in S7. A similar effect was previously observed in the heterostructure of a few layers of chromium triiodide and a single-layer WSe_2[10] but not from bulk Cr-based AFM material.

The ρ behavior as a function of B-field in $CrPS_4/WSe_2$ remains unchanged when switching from circular to linear excitation polarization (S3), indicating polarization-independent charge transfer, likely due to the anisotropic monoclinic crystal structure.[16]

We also observed excitation-power dependence in $CrPS_4$'s ρ (see S2), with ρ decreasing nonlinearly as laser power increased. This behavior can be attributed to laser-induced thermal effects that enhance spin fluctuations in $CrPS_4$. This is consistent with previous observations of temperature-dependent spin fluctuations in this material via NV magnetometry.[44]

The Zeeman energy splitting behavior of the WSe_2 intrinsic defect peak as a function of B-field is presented in Fig. 3(c). It exhibits a linear trend when $CrPS_4$ is in the A-type AFM state (Inset Fig. 3(c)), but becomes non-linear and saturates at higher B-fields. This mirrors the polarization contrast behavior in Fig. 3(b) and aligns with previously reported valley splitting in WSe_2 due to MPI with FM substrate europium sulfide.[45]

Next, we studied both circularly polarization-weighted intensity components as functions of B-field for the $CrPS_4$ emission line at 1.355 eV (Fig. 4(a), backward B-field sweep). A

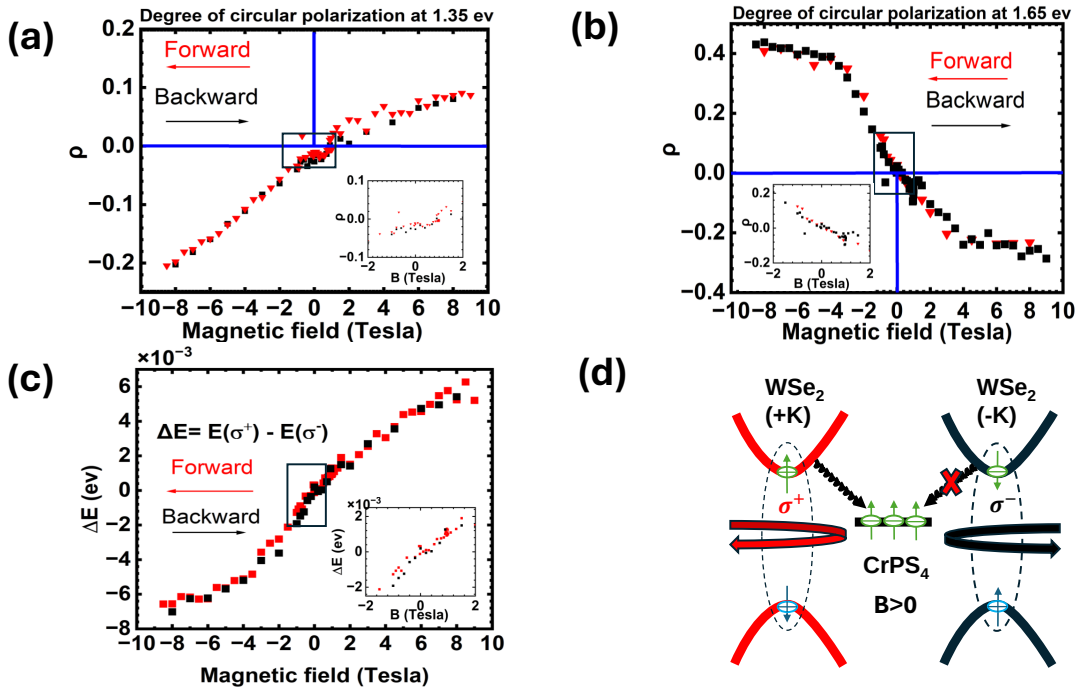


Figure 3: The ρ and Zeeman splitting measurements as a function of B-fields: (a) The ρ measurement of one of the peaks of $CrPS_4$ centered around 1.355 eV as a function of B-fields, with arrows indicating the direction of the magnetic sweep, inset in (a) is ρ focusing on the A-type AFM state of $CrPS_4$. (b) The ρ measurement of the intrinsic defect peak of WSe_2 centered around 1.65 eV as a function of B-fields, the inset in (b) shows the ρ of the intrinsic defect peak in WSe_2 when $CrPS_4$ is in A-type AFM state. (c) The Zeeman splitting of the defect peak of WSe_2 centered around 1.65 eV as a function of B-fields, the inset in (c) shows the Zeeman splitting of the intrinsic defect peak in WSe_2 when $CrPS_4$ is in A-type AFM state. (d) A schematic demonstrating the spin-polarized charge transfer effect in the heterostructure due to type-II band alignment.

constant gap between the polarization components appears when $CrPS_4$ is in the A-type AFM state (Fig. 4(b)). Both components show anisotropic behavior in the positive field regime compared to the negative field regime (Fig. 4(a)). suggesting the anisotropy could arise from crystal symmetry breaking in the AFM structure. Similar trends were observed in the forward B-field sweep direction as well (not shown).

Although Parity-Time (PT) symmetry predicts equal polarization component behavior in the A-type AFM regime and isotropic behavior in the C-AFM state, the observed anisotropy may result from PT symmetry breaking due to the introduction of WSe_2 atop $CrPS_4$. Notably, WSe_2 atop a magnetic material is known to induce a strong Rashba effect,

significantly altering the surface magnetic textures.[46] Further studies, such as spin-polarized scanning tunneling microscopy (STM) as a function of B-field and $CrPS_4$ thickness, with or without WSe_2 atop, are needed to clarify this behavior. Nevertheless, such a robust polarization gap in the A-type AFM state (Fig. 4(a)) highlights the potential of interfacial symmetry engineering for ultrafast AFM memory devices, where optically controlled anisotropy could enable non-volatile operation.

In addition to experimental analysis, we also performed DFT calculations to gain better insights into the electronic structure of both $CrPS_4$ and its heterostructure with WSe_2. As shown in Fig. 4(c), $CrPS_4$ exhibits a monoclinic crystal structure with anisotropy along the crystal axes directions a and b, resulting in ferromagnetic ground states within each layer, and antiferromagnetically coupled interactions between adjacent layers. The magnetic moment per Cr atom in a single layer is found to be 2.85 μ_B, consistent with the previously calculated value.[15] The b vector is normal to the ac plane while the a and c vectors are at an angle of approximately 92 degrees, owing to the monoclinic crystal structure with C_2 rotational symmetry of $CrPS_4$.

Further, we present the band diagram of bulk $CrPS_4$ with and without spin-orbit coupling (S4 (c) and S4 (d)), which shows no significant difference. The negligible spin-orbit coupling in $CrPS_4$ explains the absence of resolvable Zeeman splitting in its optical transitions, indicating that these transitions are localized.

Fig. 4(d) presents the calculated band gaps of few-layer to bulk $CrPS_4$, as well as WSe_2 with and without spin-orbit coupling. The band alignment between $CrPS_4$ and WSe_2 remains type-II irrespective of $CrPS_4$ thicknesses. This alignment is further confirmed by the band diagram of monolayer $CrPS_4$ and WSe_2 heterostructure (S4 (f) and S4 (g)), where the highlighted bands clearly illustrate the type-II alignment. Additional details on the DFT calculations are provided in the supplementary information.

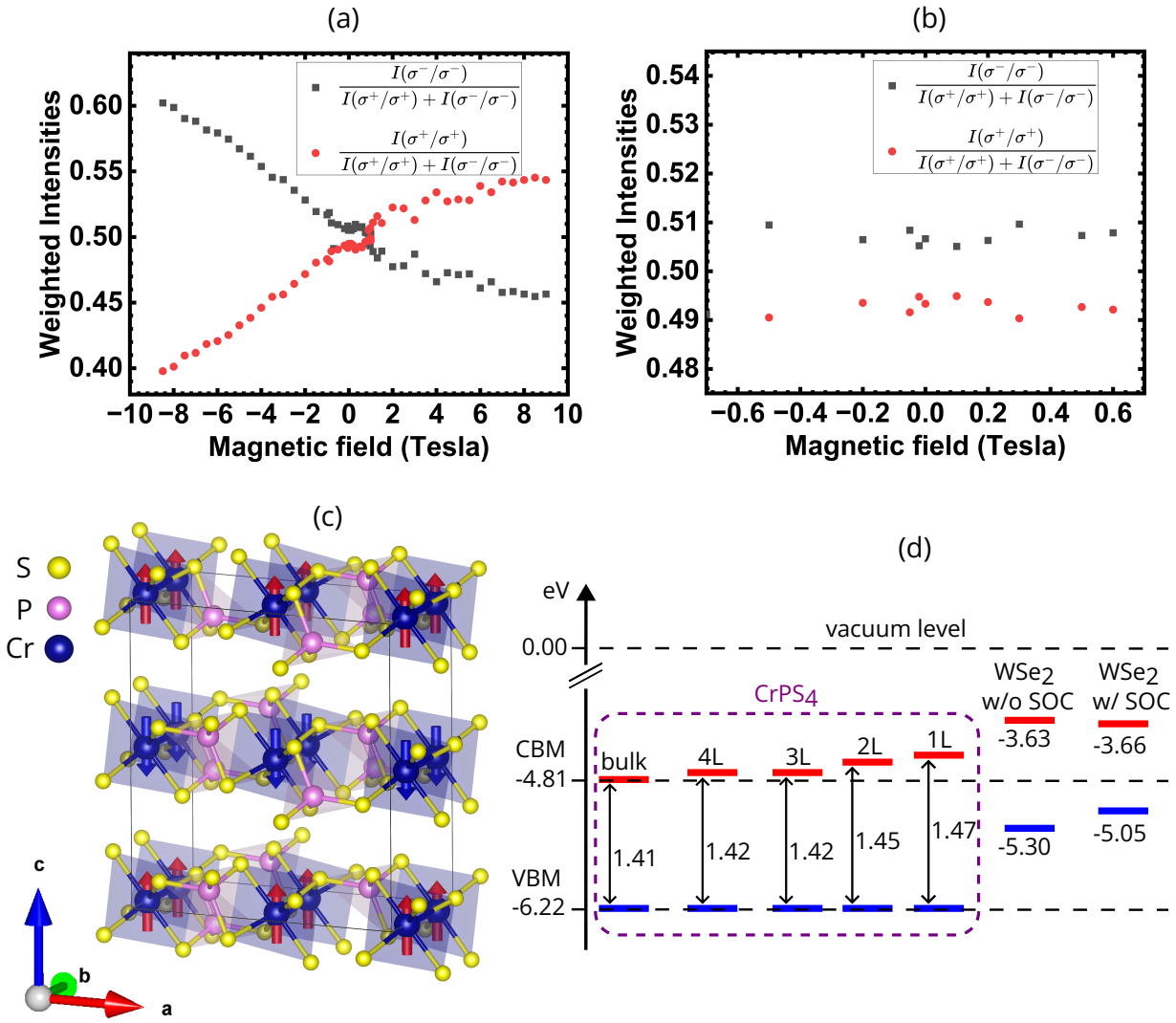


Figure 4: (a) Shows the weighted intensities of the polarization component of one of the $CrPS_4$ peaks at 1.355 eV during the backward magnetic sweep measurements, providing insights into the polarization behavior of the emitted light as a function of B-fields. (b) Zoomed-in image of (a), focusing specifically on a range corresponding to the A-type AFM state in $CrPS_4$, allows for a detailed examination of the polarization characteristics within this magnetic regime. (c) The crystal structure of $CrPS_4$, as determined by DFT, and offers a visual representation of its atomic arrangement and symmetry properties. (d) The electronic structures of $CrPS_4$ across varying layer thicknesses, ranging from monolayer to bulk, along with comparisons to that of WSe_2 with and without spin-orbit coupling, further confirming the type-II band alignment of $CrPS_4$ and WSe_2 heterostructure.

Conclusion

In conclusion, we present a method for analyzing the A-type AFM and C-AFM states in optically active 2D bulk semiconductor magnets. Additionally, we successfully detected the

surface layer magnetic moment of $CrPS_4$ by utilizing WSe_2 defect states in a magnetic heterostructure. Our prediction of type-II band alignment through DFT calculations supports the observed spin-polarized charge transfer in the heterostructure of bulk $CrPS_4$ and single-layer WSe_2. Due to its anisotropic monoclinic structure, the spin-polarized charge transfer in heterostructures remains independent of excitation polarization. Overall, our work highlights the potential of utilizing optically active bulk 2D AFM material as ultrafast optical memory storage devices by using its surface layer properties. Furthermore, owing to spin-polarized charge transfer, TMDC-based heterostructures emerge as promising candidates for quantum information processing.

Method

Heterostructure preparation

For preparing the heterostructure, $CrPS_4$, WSe_2, and hexagonal boron nitride (hBN) flakes were cleaved out from the bulk using less residual tape. Then the flakes are further cleaved into thinner portions using the tape multiple times. For $CrPS_4$, the thinner flakes in the tape are pressed into the Si/SiO_2 substrate, and for WSe_2 and hBN, the flakes are pressed into Polydimethylsiloxane (PDMS) after removing the tape, multiple flakes are transferred into the Si/SiO_2 substrate and PDMS. The bulk $CrPS_4$ and single-layer WSe_2 were identified by optical microscope using optical contrast from the flake and further confirmed by Raman and PL spectroscopy. The heterostructure was prepared by stacking flakes together using PC and transferred into the marked substrate for PL measurements.

Magneto-photoluminescence

The sample was positioned inside the Attocube-2100 cryostat with the superconducting magnet in Faraday geometry, range up to ± 9 Tesla, equipped with a confocal microscope head placed on top of the cryostat to conduct polarized resolved photoluminescence measurements

as a function of B-field and temperature. The cryostat objective, featuring a numerical aperture (NA) of 0.82, was utilized to facilitate the excitation of the sample using a 532 nm continuous wave laser. The cryostat objective provided a spot size of ∼791.5 nm, ensuring accurate focusing of the laser beam onto the sample. Circularly polarized light (σ^+ and σ^-) was generated and detected by the combination of a linear polarizer and a quarter-wave plate from Thorlabs. To capture the emitted light, the collection arm of the microscope was connected to a fiber-optic cable, which directed the light to the entrance port of the Teledyne HRS-750 triple-grating imaging spectrometer. The spectrometer, with a focal length of 750 mm, enabled efficient spectral analysis. Subsequently, the collimated light was diffracted from the grating within the spectrometer and directed toward a nitrogen-cooled CCD camera. The camera featured a pixel array configuration of 1340x400, which facilitated precise and detailed spectral measurements.

.

Associated Content

Data availability statement

The data that support the findings of this study are available from the author upon reasonable request. The pre-print version of this manuscript is available on arXiV: M.H. Shaikh, M.P. Whalen, Dai Q. Ho, A. Ishraq, C. Maurtua, K. Watanabe, T. Taniguchi, Y. Ren, A. Janotti, J.Q. Xiao, C. Chakraborty. Magnetic proximity coupling to defects in a two-dimensional semiconductor (2024), 2408.11986:arXiv, DOI:10.48550/arXiv.2408.11986 (accessed on Aug 21, 2024).

Supporting information available

Computational method for DFT calculation, room temperature co-polarization resolved PL of $CrPS_4$ and WSe_2 heterostructure, power-dependent degree of circular polarization mea-

surement at −8 Tesla, magnetic sweep measurement of heterostructure with excitation of different polarization, electronic structure of bulk $CrPS_4$ and heterostructure between its monolayer and WSe_2, Example of peak fitting of intrinsic defect states and excitonic transition using Lorentzian function, Spectral fitting of the DBE exciton from Fig 1(e), Degree of circular polarization of DBE excitons as a function of B-field, polarization-resolved PL and absolute polarization contrast of DBE exciton as a function of temperature, Excitation dependent polarization resolved PL of DBE and spatially resolved PL of DBE.

Contribution

The measurements and characterization were done by M.H.S. The device fabrication was done by M.H.S and M.P.W. The theoretical calculations were performed by D.Q.H, supervised by A.J. J.Q.X., Y.R., C.C., and M.H.S. contributed to the interpretation of data. C.C. supervised the project and wrote the draft together with M.H.S. All authors contributed to the manuscript preparation and approved its final version.

Acknowledgement

This research was partially supported by the National Science Foundation (NSF) through the University of Delaware (UD) Materials Research Science and Engineering Center (MRSEC) DMR-2011824 Seed Award program. M.H.S., A.I., C.M., A.J., and C.C. acknowledge partial support by the NSF Award OIA-2217786. M.P.W. and J.Q.X. acknowledge support from NSF Award No. 2203829. Y.R. acknowledges support by the UD Research Foundation Strategic Initiative Award. Y.R. also acknowledges support from NSF through the UD MRSEC DMR-2011824. A.J. and D.Q.H. also acknowledge the use of the resources of the National Energy Research Scientific Computing Center (NERSC), a Department of Energy User Facility using NERSC award No. ERCAP0034471. The authors thank Xi Wang from the Department of Material Science and Engineering, University of Delaware, for providing

access to their transfer station and room temperature PL and Raman measurement setup. The authors thank Yi Ji from the Department of Physics and Astronomy, University of Delaware, for providing access to their optical microscope.

References

(1) Zutic, I. *Spintronics Handbook: Spin Transport and Magnetism*; CRC Press, Taylor & Francis Group, 2019.

(2) Hirohata, A.; Yamada, K.; Nakatani, Y.; Prejbeanu, I.-L.; Diény, B.; Pirro, P.; Hillebrands, B. Review on spintronics: Principles and device applications. *Journal of Magnetism and Magnetic Materials* **2020**, *509*, 166711.

(3) Grollier, J.; Querlioz, D.; Camsari, K.; Everschor-Sitte, K.; Fukami, S.; Stiles, M. D. Neuromorphic spintronics. *Nature electronics* **2020**, *3*, 360–370.

(4) Jungwirth, T.; Marti, X.; Wadley, P.; Wunderlich, J. Antiferromagnetic spintronics. *Nature nanotechnology* **2016**, *11*, 231–241.

(5) Baltz, V.; Manchon, A.; Tsoi, M.; Moriyama, T.; Ono, T.; Tserkovnyak, Y. Antiferromagnetic spintronics. *Reviews of Modern Physics* **2018**, *90*, 015005.

(6) Železnỳ, J.; Wadley, P.; Olejník, K.; Hoffmann, A.; Ohno, H. Spin transport and spin torque in antiferromagnetic devices. *Nature Physics* **2018**, *14*, 220–228.

(7) Siddiqui, S. A.; Sklenar, J.; Kang, K.; Gilbert, M. J.; Schleife, A.; Mason, N.; Hoffmann, A. Metallic antiferromagnets. *Journal of Applied Physics* **2020**, *128*.

(8) McGuire, M. A. Cleavable magnetic materials from van der Waals layered transition metal halides and chalcogenides. *Journal of Applied Physics* **2020**, *128*.

(9) Basak, K.; Ghosh, M.; Chowdhury, S.; Jana, D. Theoretical studies on electronic, magnetic and optical properties of two-dimensional transition metal trihalides. *Journal of Physics: Condensed Matter* **2023**, *35*, 233001.

(10) Zhong, D.; Seyler, K. L.; Linpeng, X.; Wilson, N. P.; Taniguchi, T.; Watanabe, K.; McGuire, M. A.; Fu, K.-M. C.; Xiao, D.; Yao, W.; others Layer-resolved magnetic proximity effect in van der Waals heterostructures. *Nature nanotechnology* **2020**, *15*, 187–191.

(11) Wei, S.; Tang, X.; Liao, X.; Ge, Y.; Jin, H.; Chen, W.; Zhang, H.; Wei, Y. Recent progress of spintronics based on emerging 2D materials: CrI_3 and Xenes. *Materials Research Express* **2019**, *6*, 122004.

(12) Son, J.; Son, S.; Park, P.; Kim, M.; Tao, Z.; Oh, J.; Lee, T.; Lee, S.; Kim, J.; Zhang, K.; others Air-stable and layer-dependent ferromagnetism in atomically thin van der Waals $CrPS_4$. *ACS nano* **2021**, *15*, 16904–16912.

(13) Peng, Y.; Ding, S.; Cheng, M.; Hu, Q.; Yang, J.; Wang, F.; Xue, M.; Liu, Z.; Lin, Z.; Avdeev, M.; others Magnetic structure and metamagnetic transitions in the van der Waals antiferromagnet $CrPS_4$. *Advanced Materials* **2020**, *32*, 2001200.

(14) Yang, J.; Fang, S.; Peng, Y.; Liu, S.; Wu, B.; Quhe, R.; Ding, S.; Yang, C.; Ma, J.; Shi, B.; others Layer-Dependent Giant Magnetoresistance in Two-Dimensional $CrPS_4$ Magnetic Tunnel Junctions. *Physical Review Applied* **2021**, *16*, 024011.

(15) Bo, X.; Li, F.; Yin, X.; Chen, Y.; Wan, X.; Pu, Y. Magnetic structure and exchange interactions of the van der Waals $CrPS_4$ monolayer under strain: A first-principles study. *Physical Review B* **2023**, *108*, 024405.

(16) Petit, Y.; Joly, S.; Segonds, P.; Boulanger, B. Recent advances in monoclinic crystal optics. *Laser & Photonics Reviews* **2013**, *7*, 920–937.

(17) Zhang, H.; Li, Y.; Hu, X.; Xu, J.; Chen, L.; Li, G.; Yin, S.; Chen, J.; Tan, C.; Kan, X.; others In-plane anisotropic 2D $CrPS_4$ for promising polarization-sensitive photodetection. *Applied Physics Letters* **2021**, *119*.

(18) Chakraborty, C.; Goodfellow, K. M.; Dhara, S.; Yoshimura, A.; Meunier, V.; Vamivakas, A. N. Quantum-confined Stark effect of individual defects in a van der Waals heterostructure. *Nano Letters* **2017**, *17*, 2253–2258.

(19) Chakraborty, C.; Shaikh, M. H. Flatland quantum materials. 2D Photonic Materials and Devices VII. 2024; p PC1288805.

(20) Chakraborty, C.; Qiu, L.; Konthasinghe, K.; Mukherjee, A.; Dhara, S.; Vamivakas, N. 3D localized trions in monolayer WSe_2 in a charge tunable van der Waals heterostructure. *Nano Letters* **2018**, *18*, 2859–2863.

(21) Palacios-Berraquero, C.; Palacios-Berraquero, C. Atomically-thin quantum light emitting diodes. *Quantum confined excitons in 2-dimensional materials* **2018**, 71–89.

(22) Chakraborty, C.; Kinnischtzke, L.; Goodfellow, K. M.; Beams, R.; Vamivakas, A. N. Voltage-controlled quantum light from an atomically thin semiconductor. *Nature nanotechnology* **2015**, *10*, 507–511.

(23) Linhart, L.; Paur, M.; Smejkal, V.; Burgdörfer, J.; Mueller, T.; Libisch, F. Localized intervalley defect excitons as single-photon emitters in WSe_2. *Physical review letters* **2019**, *123*, 146401.

(24) Shepard, G. D.; Ajayi, O. A.; Li, X.; Zhu, X.; Hone, J.; Strauf, S. Nanobubble induced formation of quantum emitters in monolayer semiconductors. *2D Materials* **2017**, *4*, 021019.

(25) Chakraborty, C.; Vamivakas, N.; Englund, D. Advances in quantum light emission from 2D materials. *Nanophotonics* **2019**, *8*, 2017–2032.

(26) Moon, H.; Grosso, G.; Chakraborty, C.; Peng, C.; Taniguchi, T.; Watanabe, K.; Englund, D. Dynamic exciton funneling by local strain control in a monolayer semiconductor. *Nano letters* **2020**, *20*, 6791–6797.

(27) Chakraborty, C.; Goodfellow, K. M.; Vamivakas, A. N. Localized emission from defects in $MoSe_2$ layers. *Optical Materials Express* **2016**, *6*, 2081–2087.

(28) Moon, H.; Bersin, E.; Chakraborty, C.; Lu, A.-Y.; Grosso, G.; Kong, J.; Englund, D. Strain-correlated localized exciton energy in atomically thin semiconductors. *ACS Photonics* **2020**, *7*, 1135–1140.

(29) Mukherjee, A.; Shayan, K.; Li, L.; Shan, J.; Mak, K. F.; Vamivakas, A. N. Observation of site-controlled localized charged excitons in CrI3/WSe2 heterostructures. *Nature Communications* **2020**, *11*, 5502.

(30) Liu, Y.; Liu, C.; Ma, Z.; Zheng, G.; Ma, Y.; Sheng, Z. annealing effect on photoluminescence of two-dimensional WSe_2/BN heterostructure. *Applied Physics Letters* **2020**, *117*.

(31) Hu, W.; Wang, Y.; He, K.; He, X.; Bai, Y.; Liu, C.; Zhou, N.; Wang, H.; Li, P.; Ma, X.; others Straining of atomically thin WSe_2 crystals: Suppressing slippage by thermal annealing. *Journal of Applied Physics* **2022**, *132*.

(32) Xie, L.; Du, L.; Lu, X.; Yang, R.; Shi, D.; Zhang, G. A facile and efficient dry transfer technique for two-dimensional Van der Waals heterostructure. *Chinese Physics B* **2017**, *26*, 087306.

(33) Srivastava, A.; Sidler, M.; Allain, A. V.; Lembke, D. S.; Kis, A.; Imamoğlu, A. Valley Zeeman effect in elementary optical excitations of monolayer WSe_2. *Nature Physics* **2015**, *11*, 141–147.

(34) Kim, S.; Yoon, S.; Ahn, H.; Jin, G.; Kim, H.; Jo, M.-H.; Lee, C.; Kim, J.; Ryu, S. Photoluminescence path bifurcations by spin-flip in two-dimensional $CrPS_4$. *ACS nano* **2022**, *16*, 16385–16393.

(35) Kumar, S.; Kaczmarczyk, A.; Gerardot, B. D. Strain-induced spatial and spectral isolation of quantum emitters in mono-and bilayer WSe_2. *Nano letters* **2015**, *15*, 7567–7573.

(36) Moody, G.; Tran, K.; Lu, X.; Autry, T.; Fraser, J. M.; Mirin, R. P.; Yang, L.; Li, X.; Silverman, K. L. Microsecond valley lifetime of defect-bound excitons in monolayer WSe_2. *Physical review letters* **2018**, *121*, 057403.

(37) Wagner, J.; Kuhn, H.; Bernhardt, R.; Zhu, J.; Van Loosdrecht, P. H. Trap induced long exciton intervalley scattering and population lifetime in monolayer WSe_2. *2D Materials* **2021**, *8*, 035018.

(38) Wang, Q.; Maisch, J.; Tang, F.; Zhao, D.; Yang, S.; Joos, R.; Portalupi, S. L.; Michler, P.; Smet, J. H. Highly polarized single photons from strain-induced quasi-1D localized excitons in WSe_2. *Nano letters* **2021**, *21*, 7175–7182.

(39) Koperski, M.; Nogajewski, K.; Arora, A.; Cherkez, V.; Mallet, P.; Veuillen, J.-Y.; Marcus, J.; Kossacki, P.; Potemski, M. Single photon emitters in exfoliated WSe_2 structures. *Nature nanotechnology* **2015**, *10*, 503–506.

(40) Srivastava, A.; Sidler, M.; Allain, A. V.; Lembke, D. S.; Kis, A.; İmamoğlu, A. Optically active quantum dots in monolayer WSe_2. *Nature nanotechnology* **2015**, *10*, 491–496.

(41) He, Y.-M.; Clark, G.; Schaibley, J. R.; He, Y.; Chen, M.-C.; Wei, Y.-J.; Ding, X.; Zhang, Q.; Yao, W.; Xu, X.; others Single quantum emitters in monolayer semiconductors. *Nature nanotechnology* **2015**, *10*, 497–502.

(42) Yang, L.; Yuan, Y.; Fu, B.; Yang, J.; Dai, D.; Shi, S.; Yan, S.; Zhu, R.; Han, X.;

Li, H.; others Revealing broken valley symmetry of quantum emitters in WSe_2 with chiral nanocavities. *Nature Communications* **2023**, *14*, 4265.

(43) Dang, J.; Sun, S.; Xie, X.; Yu, Y.; Peng, K.; Qian, C.; Wu, S.; Song, F.; Yang, J.; Xiao, S.; others Identifying defect-related quantum emitters in monolayer WSe_2. *npj 2D Materials and Applications* **2020**, *4*, 2.

(44) Huang, M.; Green, J. C.; Zhou, J.; Williams, V.; Li, S.; Lu, H.; Djugba, D.; Wang, H.; Flebus, B.; Ni, N.; others Layer-dependent magnetism and spin fluctuations in atomically thin van der Waals magnet $CrPS_4$. *Nano Letters* **2023**, *23*, 8099–8105.

(45) Zhao, C.; Norden, T.; Zhang, P.; Zhao, P.; Cheng, Y.; Sun, F.; Parry, J. P.; Taheri, P.; Wang, J.; Yang, Y.; others Enhanced valley splitting in monolayer WSe_2 due to magnetic exchange field. *Nature nanotechnology* **2017**, *12*, 757–762.

(46) Dolui, K.; Nikolić, B. K. Spin-orbit-proximitized ferromagnetic metal by monolayer transition metal dichalcogenide: Atlas of spectral functions, spin textures, and spin-orbit torques in Co/$MoSe_2$, Co/WSe_2, and Co/$TaSe_2$ heterostructures. *Physical Review Materials* **2020**, *4*, 104007.